This is a preprint, the final version is subject to change, of the American Mineralogist (MSA)
Cite as Authors (Year) Title. American Mineralogist, in press.
DOI: https://doi.org/10.2138/am-2018-6382

# Running title: Fe oxidation in amphiboles

# Revision 1

# The dynamics of Fe oxidation in riebeckite:

# a model for amphiboles

**GIANCARLO DELLA VENTURA[1,2*], BORIANA MIHAILOVA[3], UMBERTO SUSTA[1], MARIANGELA CESTELLI GUIDI[2], AUGUSTO MARCELLI[2,4], JOCHEN SCHLÜTER[5] AND ROBERTA OBERTI[6]**

*[1]Department Sciences, University of Roma Tre, Rome, Italy*

*[2]LNF-INFN, Frascati (Rome), Italy*

*[3]Fachbereich Geowissenschaften, Universität Hamburg, Hamburg, Germany*

*[4]RICMASS, Rome International Center for Materials Science Superstripes, Rome, Italy*

*[5]Centrum für Naturkunde, Universität Hamburg, Hamburg, Germany*

*[6]CNR-Istituto di Geoscienze e Georisorse, Pavia, Italy*

*** Correspondence:**

Giancarlo Della Ventura

giancarlo.dellaventura@uniroma3.it

## ABSTRACT

In this work we investigate the oxidation behavior of a nearly end-member riebeckite, ideally $Na_2(Fe^{2+}_3Fe^{3+}_2)Si_8O_{22}(OH)_2$, by using vibrational FTIR and Raman spectroscopies. Combining these results with previous studies done on the same sample by single-crystal structure refinement and Mössbauer spectroscopy, we conclude that iron oxidation in riebeckite is a multi-step process: (i) in the ~523 K < *T* < 623 K temperature range, the O-H bond lengthens and both the electrons and the hydrogen cations delocalize; Raman analysis shows that this step is reversible upon cooling to room-temperature; (ii) in the 623 K< *T* < 723 K range, the kinetic energy increases so that the electrons can be ejected from the crystal; beyond 723 K an irreversible oxidation of Fe occurs that couples with irreversible changes in the $SiO_4$ double-chains leading to a contraction of the unit-cell volume, i.e., to structural changes detectable at the long-range scale; (iii) beyond 823 K, the irreversible oxidation is completed and $H^+$ ions are forced to leave the crystal bulk. Because of this multi-step process, the onset of the deprotonation process is detected at ~700 K by single-crystal XRD analysis of the unit-cell parameters, but starts at 623 K as indicated by Mössbauer spectroscopy on powders (and by changes in the cation distribution observed by structure refinement). Also, Raman scattering shows that the release of $H^+$ from the crystal surface starts ~100 K before the complete deprotonation of the crystal bulk is witnessed by FTIR absorption. Hence, the oxidation of Fe starts at the crystal surface and induces electron and $H^+$ migration from the crystal interior to the rim and thus subsequent oxidation through the crystal bulk. No deprotonation is observed by FTIR either in powders embedded in KBr or in crystals heated in $N_2$ atmosphere, implying that the release of $H^+$ needs surficial (atmospheric) oxygen to form $H_2O$ molecules. $Fe^{2+} \rightarrow Fe^{3+}$ oxidation produces a flux of electrons throughout the crystal matrix, which generates electrical conductivity across the amphibole. An important implication of this work, which might have interesting applications in material science, is that iron oxidation in riebeckite (and possibly in other Fe-rich silicates) is reversible in a given

range of temperature. Also, this work shows that complex processes cannot be fully understood or even monitored accurately without using a proper combination of independent techniques.

**Keywords: riebeckite, H*T* spectroscopy, FTIR, Raman, iron oxidation, deprotonation.**

## INTRODUCTION

Mineral reactions of hydrous materials at high temperatures (H*T*) involve loss and migration or diffusion of hydrogen (e.g., Aines and Rossman 1985; Zang et al. 2005, 2006; Della Ventura et al. 2015a, 2015b). These processes may be associated with simultaneous oxidation of multi-valence elements, typically Fe or Mn, with significant consequences on the physical properties of the material, such as the electrical conductivity or magnetic properties.

Among rock-forming minerals, a notable case is provided by amphiboles. Iron-dominant sodic amphiboles ("crocidolites") were extensively studied at H*T* during the 1960-1970's (Addison et al. 1962a 1962b; Addison and Sharp 1962, 1968; Hodgson et al. 1965; Addison and White 1968; Ernst and Wai 1970) because of their technological applications, the most important of which was insulation from heat and fire. The general features of the deprotonation mechanism were sketched during these early studies (e.g., Addison and Sharp 1962a), but the structural adjustments accompanying the oxidation of iron and the loss of hydrogen were addressed later (Ungaretti 1980; Clowe et al. 1988; Phillips et al. 1988, 1989, 1991). Despite these efforts, notable issues still need to be understood, in particular the dynamics of iron oxidation and the diffusion throughout the mineral matrix of the electrons and of the hydrogen cations produced during thermal treatment. Understanding the oxidation mechanisms of Fe-rich amphiboles, however, may have important implications in several fields of science including geology/petrology, geophysics, material science, but also medical sciences, since it is now clear that the toxic potential of mineral fibers is related to the availability and redox reactions of iron ions at the fiber surface (e.g., Turci et al. 2017).

Oberti et al. (2016) and Della Ventura et al. (2017) recently studied the H*T* behavior of synthetic potassium-ferro-richterite. Combining X-ray diffraction (XRD) and Fourier Transform Infrared (FTIR) analysis they showed that in this amphibole composition, the oxidation/deprotonation reaction starts around 620 K and ends in a relatively limited *T* range (~100 K). However, an anomalous increase of the intensities of the OH-stretching absorption

was observed during in situ measurements, and this feature could not be explained satisfactorily. Also, the difference between the onset temperatures obtained by single-crystal FTIR and XRD analysis (~100 K) was interpreted in terms of different diffusion mechanisms for $H^+$ and $e^-$, which is required for the deprotonation to proceed (Della Ventura et al. 2017). Oberti et al. (2018) studied by single-crystal XRD and Mössbauer spectroscopy the H*T* behavior of a nearly stoichiometric riebeckite characterized by Susta et al. (2018), and showed that the oxidation/deprotonation reaction starts around 700 K and takes place over a narrow temperature range also in this amphibole composition. In the present paper, we show further advancements obtained by using vibrational spectroscopies (FTIR and Raman) on the same riebeckite sample studied by Oberti et al. (2018), and propose a comprehensive model of iron oxidation and $H^+$ diffusion in amphiboles, which is based on the combination of all the data obtained with analytical methods that probe the crystal structure at different length and time scales.

## MATERIAL AND METHODS

### Studied sample

The sample used for the H*T* experiments is a riebeckite from Malawi, with crystal-chemical formula $^{A}(K_{0.06}Na_{0.04})\ ^{B}(Na_{1.82}\ Ca_{0.13}Fe^{2+}_{0.05})\ ^{C}[^{M(1)}(Fe^{2+}_{1.84}Mg^{2+}_{0.16})^{M(2)}(Fe^{2+}_{0.21}Mg^{2+}_{0.04}Fe^{3+}_{1.64}Al^{3+}_{0.10}Ti^{4+}_{0.01})\ ^{M(3)}(Fe^{2+}_{0.89}Mg^{2+}_{0.06}Mn^{2+}_{0.05})]\ ^{T}(Si_{7.97}Al_{0.03})\ O_{22}\ ^{W}((OH)^-_{1.9}F^-_{0.10})$, that is very close to the end-member composition $^{A}\square\,^{B}Na_2\,^{C}(Fe^{2+}_3Fe^{3+}_2)^{T}Si_8O_{22}\,^{W}(OH)_2$ (Susta et al. 2018). To help following the discussion, in Figure 1a we report the crystal structure of the studied sample together with the correct site nomenclature for A-, B-, C- and T-group cations and W-group anions (Hawthorne et al. 2012).

### FTIR spectroscopy

Single crystal H*T*-FTIR spectra were collected at INFN (Istituto Nazionale di Fisica Nucleare, Frascati, Rome) using a Linkam 1400XY heating stage fitted on a Bruker Hyperion 3000 FTIR microscope, equipped with a 15X Schwarzschild objective and a MCT $LN_2$-cooled detector. The microscope was attached to a Vertex 70V optical bench equipped with a KBr beamsplitter and a Globar IR source. A beam diameter of 100 μm was used for the measurements; the nominal resolution was set at 4 $cm^{-1}$ and 128 spectra were co-added for both mineral and background. Considering that there was no need to determine the absolute concentrations, but only the evolution of the OH content with *T*, the data were collected with unpolarized radiation on a randomly oriented, 135 μm thick, doubly-polished crystal section. After polishing, the section was broken into several fragments. The first fragment was used for a continuous heating ramp with a 10 K/min rate; FTIR spectra were collected in situ every 20 K just after reaching the target temperature. Because the behavior observed was quite anomalous (see below for a discussion), a second fragment was heated again with a 10 K/min rate, but FTIR spectra were collected at 50 K intervals first in situ and then after quenching to room temperature (R*T*). At any step, the temperature was restored quickly (50 K/min heating rate), and the ramp was continued at the same 10 K/min rate to the next step. This process continued until the *T* value was reached where no OH-absorption bands could be observed.

**Raman spectroscopy**

Raman spectroscopic experiments were performed with a Horiba T64000 triple monochromator system operating in a subtractive regime and equipped with a Symphony $LN_2$-cooled CCD detector and an Olympus BX41 confocal microscope. Raman scattering in the ranges 15-1215 $cm^{-1}$ and 3450-3800 $cm^{-1}$ was measured in backscattering geometry, using the 514.5-nm line of a Coherent 90C Fred $Ar^+$ laser. The laser beam was focused to a spot of linear size ~2 μm on raw natural surfaces of single crystals. The effective penetration depth was also approximately 2 μm. Polarized Raman spectra from more than 10 specimens, each

129 probed in at least three points, were collected at room temperature to verify the homogeneity
130 of the samples and the repeatability of the spectra. Two representative crystals ~2 mm ×1 mm
131 ×0.5 mm in size were selected for high-temperature experiments: S-110 and S-120, which had
132 different crystallographic orientation of the probed crystal surface: $(\bar{1}10)$ and $(\bar{1}20)$,
133 respectively. The crystal orientation was determined by X-ray diffraction using a Nonius
134 Kappa CCD singe-crystal diffractometer and MoK$\alpha$ radiation. In situ high-temperature
135 Raman experiments were done in ambient atmosphere using a Linkam TS1200 heating stage
136 attached to a T95 temperature controller, providing precision in the read-out temperature of
137 0.1 K. The crystals were aligned with their prism axis, i.e., the monoclinic *c* axis,
138 perpendicular to both the polarization and propagation direction of the laser beam. In such
139 geometry, parallel polarized spectra were obtained (where scattered-light polarization is
140 parallel to the incident-light polarization) to ensure strong Raman intensity from the OH
141 stretching modes (Leissner et al. 2016, Susta et al. 2018). Crystal S-110 was subjected to
142 three subsequent ramps: (i) heating at a 10 K/min rate with spectra collected every 50 K
143 between 373 and 723 K, and then cooling down with the same rate and collecting spectra at
144 573, 423 and 297 K (Figure 4a, lower part); (ii) heating and cooling with a 10 K/min rate and
145 with spectra collected only at three temperatures: 623, 423, and 773 K (Figure 4a, upper part);
146 (iii) cooling down to 348 K at a 50 K/min rate, followed by further cooling to 299 K at a 10
147 K/min rate, where the final spectrum was collected (Figure 4a, top line). Crystal S-120 was
148 first heated with a 50 K/min rate up to 673 K, where a spectrum was collected; then the
149 crystal was heated further with a 10 K/min rate up to 793 K, and spectra were collected every
150 10 or 25 K, and finally cooled down to R*T* under the same conditions used for crystal S-110.
151 At each temperature, data collection started after 5 min of equilibration, and the total
152 acquisition time at each temperature was approximately 15 min (Figure 4b). The preserved
153 crystallinity of the heated amphibole crystals was verified by singe-crystal X-ray diffraction at
154 the end of each experiment. The measured Raman spectra were baseline corrected with a

polynomial function to account for the continuum photoluminescence background, if any, and then normalized by the Bose-Einstein population factor for Stokes processes to remove the trivial temperature dependence of the Raman intensities: $I = I_0/(n(\omega,T)+1)$, $n(\omega,T) = 1/(e^{\eta\omega/kT}-1)$, where $\omega$, $T$, $\hbar$, and $k$ denote the phonon wavenumber, the temperature, the reduced Planck constant, and the Boltzmann constant, respectively. The temperature-reduced spectra were fitted with pseudo-Voigt functions to determine peak positions, full widths at half maximum (FWHMs) and integrated intensities.

## RESULTS

### FTIR spectroscopy in the OH-stretching region

While studying synthetic potassic-ferro-richterite, Della Ventura et al. (2017) showed that FTIR spectra in the OH-stretching region collected in situ at H*T* are significantly different from those collected on quenched samples. Similar results were obtained during this study (Figure 2). The R*T* FTIR single-crystal spectrum of untreated riebeckite consists of three main components which can be assigned to local configurations: $MgMgFe^{2+}$ (3650 $cm^{-1}$), $MgFe^{2+}Fe^{2+}$ (3637 $cm^{-1}$), and $Fe^{2+}Fe^{2+}Fe^{2+}$ (3618 $cm^{-1}$; Susta et al. 2018). The very minor component at 3667 $cm^{-1}$ (which was not present in Susta et al. 2018) can be assigned to the MgMgMg local configuration, and can be explained both by a slight compositional inhomogeneity and by the greater thickness of the crystal used in this work (135 vs. 26 μm), which aims at maximizing the OH-signal during the H*T* data collection.

Figure 2a shows the spectra collected[1] on samples quenched after heating at different *T*. No change in the shape and the intensity of the peaks is visible below 833 K. A slight intensity decrease can be observed between 833 and 873 K, whereas no signal of the presence of OH groups is preserved at 893 K. The integrated IR absorbance in the 3680-3580 $cm^{-1}$

[1] Original FTIR and Raman spectra are available upon request to the first author

range is constant up to 853 K (Fig. 3), similar to the relative IR absorbance of the individual components and their FWHM. In the 853 K < *T* < 873 K range there is a significant decrease in the integrated intensity, which becomes zero at 893 K.

The evolution of the IR spectra collected in situ (Fig. 2b) shows that all bands progressively shift toward lower wavenumbers and broaden significantly while increasing *T*, which is the behavior expected for phonons in crystals with a positive thermal expansion. However, an evident and anomalous increase in the band intensity is observed at higher temperatures. Because of the *T*-induced band broadening, the three main components, which are well resolved in the R*T* spectrum, can no longer be recognized at *T* > 723 K. Figure 3 shows that the temperature dependence of the integrated IR absorption collected in situ differs from that observed for those collected after quenching, showing a strong increase with increasing *T*. As already observed for potassic-ferro-richterite (Della Ventura et al. 2017) this increase is not linear with *T*, but runs up significantly when approaching the onset of deprotonation.

Interestingly, heating experiments done on powders using the conventional KBr-pellet technique did not register any $H^+$ loss, independent on the rate of the heating ramp and the duration of the experiment. Similarly, no $OH^-$ loss was observed while heating single-crystals in $N_2$ atmosphere. In contrast, $H^+$ loss was clearly observed when using pure amphibole powders deposited on the sample holder. All these evidences suggest that deprotonation in amphiboles is essentially a surface phenomenon which requires the presence of external $O_2$ (Addison et al. 1962a; Della Ventura et al. 2017); this point will be further discussed below.

**Raman spectroscopy**

Figure 4 shows the results obtained on both the S-110 and S-120 crystals at different temperatures. The initial R*T* spectra of the two samples show a slight difference in the relative peak intensities due to the different orientation of the crystallographic *a* and *b* axes with

respect to the polarization of the incident light (as explained above) and the consequent variation in the Raman polarizability tensor. This orientation dependence is more pronounced in the range of framework vibrations (Leissner et al. 2015; Susta et al. 2018), but does not affect the analysis of structural/chemical changes induced by temperature because for each sample the scattering geometry was kept constant during the experiment.

For both samples, the OH-stretching Raman scattering near 3619 $cm^{-1}$ disappears at 723 K during the first heating ramp (Fig. 4), indicating the loss of $H^+$ from the O(3) anion site. In the same *T* interval, the 146 and 165 $cm^{-1}$ bands decrease in intensity, while the band at 173 $cm^{-1}$ increases (see enlargements in Fig. 5). The spectral range 100-250 $cm^{-1}$ are dominated by *M*-O vibrations (Susta et al. 2018); therefore these changes have to be assigned to the $^{C}Fe^{2+} \rightarrow {}^{C}Fe^{3+}$ oxidation. Mössbauer data collected on the same sample during thermal annealing (Oberti et al. 2018) had shown that Fe oxidation occurs only at the *M*(1) site, whereas $^{M(3)}Fe^{2+}$ is unaffected. Thus, the intensity reduction of the Raman peak near 146 $cm^{-1}$ and the change in the intensity ratio of the peaks at 165 and 173 $cm^{-1}$ are directly related to the oxidation of $^{M(1)}Fe^{2+}$ to $^{M(1)}Fe^{3+}$.

Crystal S-110 was cooled down immediately after reaching 723 K, and a striking effect was observed, namely, a complete recovery of both the OH stretching at 3619 $cm^{-1}$ and the $^{M(1,3)}Fe^{2+}$-O stretching at 146-165 $cm^{-1}$ (Fig. 4 and 5). A subsequent reheating to 623 K followed by cooling to 423 K confirmed the reversibility of the transition at *T* values lower than 723 K (Fig. 4). Only after heating the sample at 773 K, the irreversible $^{W}OH^- + {}^{M(1)}Fe^{2+} \rightarrow {}^{W}O^{2-} + {}^{M(1)}Fe^{3+}$ redox reaction could be obtained (Fig. 4). Similarly to S-110, the Raman scattering of S-120 arising from OH stretching as well as that near 146 and 165 $cm^{-1}$ disappear at 723 K. However, because crystal S-120 had been gradually heated up to 798 K, the observed changes are irreversible on cooling at the end of the experiment (Fig. 4). Interestingly, above 723 K the background of inelastic-light scattering drastically increases,

indicating the presence of a large number of mobile charge carriers (namely, electrons in the conduction band) inside the crystal.

## DISCUSSION

The deprotonation reaction in Fe-bearing amphiboles can be expressed as (Addison and Sharp 1962a; Phillips et al. 1988):

$$4Fe^{2+} + 4OH^{-} + O_2 = 4Fe^{3+} + 4O^{2-} + 2H_2O \qquad (1).$$

According to this equation, the oxidation of iron is balanced by the loss of $H^+$ ions bonded to the O(3) oxygen atom, which then combine with oxygen to produce water. Note that four electrons are also released during the above reaction.

The spectroscopic experiments described in this paper provide further insights into the deprotonation reaction, which is probably one of the most important processes in geology due to its consequences both on the H*T* stability of rock-forming silicates (e.g., micas and amphiboles), and the release of fluids in mantle environments.

The first and perhaps more interesting issue is that the deprotonation process is not straightforward. Raman experiments on sample S-110 (Fig. 4, left) clearly show that up to $T \sim$ 723 K all $H^+$ ions are delocalized because any sign of O-H stretching scattering is lost and, simultaneously, adjacent $^{M(1)}Fe^{2+}$ cations loose one electron to maintain the local charge balance, as schematically shown in Figure 1b. However, this stage is still reversible because both the OH groups and the $^{M(1)}Fe^{2+}$ oxidation state can be recovered on cooling. Hence, up to this $T$ value both $H^+$ and $e^-$ must remain within the crystal matrix. Only at 773 K the kinetic energy of the delocalized $H^+$ and $e^-$ is high enough to eject them from the crystal, leading to irreversible changes in the valence-state at the O(3) and *M*(1) sites. It is worth mentioning that a partial recovery of $OH^-$ groups and ferrous iron had already been noted in the case of $Fe^{2+}$-rich tourmaline subjected to heating in air (Watenphul et al. 2017).

Second, our data indicate that the deprotonation process cannot be monitored correctly by in situ measurements; a strong increase in molar absorption is in fact obtained (Fig. 2 and 3), in apparent disagreement with what expected for a deprotonation. Della Ventura et al. (2017) had already noted the same trends in synthetic potassic-ferro-richterite, but could not provide sound explanations. In this work we can use the information provided by Raman analysis of the OH-stretching modes, of the *M*(1)-O modes, as well as of $SiO_4$-ring mode near 665 $cm^{-1}$ and of the $SiO_4$ stretching mode near 971 $cm^{-1}$ to get a further insight into this process.

Fig. 6a and 6d show that the integrated intensity of the OH-stretching bands collected on crystal S-110 and S-120 (respectively) during the first heating ramp peaks before decreasing quickly, similarly to what is observed for the intensity of the OH stretching measured in situ by FTIR (Fig. 3). We can now explain this apparent increase by the enlarged amplitudes of hydrogen atomic vector displacements in the OH-stretching mode (in both FTIR and Raman spectra) during $H^+$ delocalization. The different response (intensity) between IR and Raman is due to the different probing methods typical of these two analytical techniques. In FTIR spectroscopy only vibrations that result in a change of the dipole moment of the molecule are observed, and strong IR absorption lines correspond to strong dipole moments. The cross section thus reflects the number of absorbing bonds in a sample at the specific wavelengths of the mid-IR radiation. Differently, Raman spectroscopy detects the inelastic scattering processes occurring in the components of the sample probed by a monochromatic laser light. As a consequence, the signal associated with Raman excitations is weak, because only about one photon over $10^6$ is inelastically scattered. An additional reason for the strong difference between the intensity increase at H*T* is also due to the different size of the sample volume probed by FTIR and Raman, respectively. In the former case the beam spot on the sample surface has a linear size of ~100 μm while in the latter case ~2 μm. The Raman-scattering penetration depth is similar to the lateral resolution, while the whole sample

thickness is probed by FTIR transmission spectroscopy. Therefore sample volume probed in our FTIR experiments is several orders of magnitude larger than that in Raman experiments.

The maximum in the Raman intensity is narrower and occurs at a higher temperature (more than 100 K) for S-120 than for S-110. This difference most probably reflects the different kinetics of heating used: sample S-120 was heated up to 573 K with a much higher rate, without collecting Raman spectra, which suggests a more abrupt processes and less thermal energy accumulated at 573 K in crystal S-120 than in crystal S-110. The trend observed for S-110 during the first cooling as well as during the second ramp does not show any surplus in the OH-stretching intensity probably because the re-bonding of mobilized $H^+$ to $^{O(3)}O^{2-}$ does not involve extra vibrational energy.

The intensity of the Raman-active $^{M(1)}Fe^{2+}$-O modes at 146 $cm^{-1}$ (Fig. 6b and 6e) and 165 $cm^{-1}$ (Fig. 6c and 6f) also peaks during the first heating ramp, and gradually recover during the reversal. This increase can be assigned to the higher vibrational energy of the *M*(1)-O bonds during Fe oxidation and to the reduction in volume of the *M*(1) octahedron (<*M*(1)-O> decrease from 2.114 to 2.043 Å; Oberti et al. 2018) due to the smaller size of the $Fe^{3+}$ cation. The maxima in both trends indicate the onset temperature of Fe oxidation and thus of electron delocalization from the $^{M(1)}Fe^{2+}$ cation. For crystal S-110 the maximum in $I_{n\,146,165\mathrm{cm}^{-1}}(T)$ (where $I_n$ is the intensity of the 146 and 165 $cm^{-1}$ bands, respectively, normalized to the total intensity in the 15-1215 $cm^{-1}$ spectral range) is at 623 K, while for crystal S-120 it is at 648 K. These values match very well the temperature of onset for $^{M(1)}Fe$ oxidation provided by Mössbauer spectroscopy (~ 623 K: Oberti et al. 2018). The slight difference (25 K) measured on the two samples may also derive from the different heating rates used. Evolution of the Raman intensities related to vibrations in the *M*(1) octahedron (Fig. 6) further confirms that in both crystals the process of $e^-$ delocalization is completed at 723 K, similar to $H^+$ delocalization.

306 The temperature dependence of the wavenumbers and of the FWHMs of selected
307 phonon modes involving $SiO_4$ vibrations confirms that, at a local scale, the changes in the
308 structural framework occurs before the $H^+$ loss is complete (Fig. 7). The wavenumber
309 evolution of the $SiO_4$-ring breathing mode near 665 $cm^{-1}$ has a clear minimum at 623 K for S-
310 110 (Fig. 7a) and at 648 K for S-120 (Fig. 7c), indicating a change in ring geometry to adjust
311 for the smaller *M*(1) octahedron. The minimum of $\omega_{665\ cm^{-1}}$is accompanied by an abrupt
312 increase in the peak width $\Gamma_{665\ cm^{-1}}$. The $SiO_4$-stretching mode near 971 $cm^{-1}$ also shows a
313 considerable steep increase of the FWHM $\Gamma_{971\ cm^{-1}}$ between 623 and 723 K for S-110 (Fig.
314 7b) and between 648 and 723 K for S-120 (Fig. 7d). The peak near 971 $cm^{-1}$ is assigned to Si-
315 $O_{nb}$ (nb = non-bridging) stretching modes because in chain silicates such modes give strong
316 Raman peaks due to their relatively high bond polarizability (Dowty 1987). Therefore, the
317 abrupt increase in the FWHM of the 971 $cm^{-1}$ peak indicates larger dispersion of the Si-$O_{nb}$
318 bond lengths, which in turn can be related to an increase in the short-range disorder at the
319 octahedral strips, once $H^+$ and $e^-$ are irreversibly released.
320 The Raman data collected from S-110 on cooling also demonstrate that the structural
321 changes within the silicate tetrahedron are reversible, although the recovery of the $SiO_4$-ring
322 geometry has a considerable temperature hysteresis.
323 From the observations described above, we can conclude that a reversible metastable
324 quasi-oxidized state of riebeckite occurs in the range 623–723 K, which is characterized by
325 the presence of charge carriers in the form of delocalized $H^+$ and $e^-$ and by atomic
326 rearrangements in the silicate chains and in the *M*(1) octahedron. The upper temperature limit
327 of this metastable state matches very well the onset temperature of deprotonation as detected
328 by a decrease in unit-cell parameters by in-situ H*T* single-crystal XRD experiments (Oberti et
329 al., 2018). According to the Raman data, the irreversible $^{W}OH^- + {}^{M(1)}Fe^{2+} \rightarrow {}^{W}O^{2-} + {}^{M(1)}Fe^{3+} +$
330 1/2 $H_2$ redox reaction occurs at 773 K, when the delocalized $H^+$ and $e^-$ gain enough kinetic
331 energy to leave the crystal.

FTIR spectra collected in transmission mode on crystal S-110 treated at 773 K still show an intense OH-stretching signal. Therefore, the reaction at this temperature is limited to the crystal surface, i.e., to the layer of few μm thickness probed by Raman spectroscopy. The Raman spectrum collected at the final temperature after cooling the deprotonated crystal shows a significant broadening, which is indicative of local chemical and/or structural disorder. Final R*T* spectra collected on crystal S-120, which was heated up to 798 K, show very broad asymmetric Raman bands near 145, 285 and 385 $cm^{-1}$, the intensity of which is enhanced, as well as changes in the relative intensities of the peaks in the range 500-1100 $cm^{-1}$, which are related to $SiO_4$ modes (see Fig. 4). This evidence might be interpreted by (irreversible or quenched) cation disorder at the B and C sites at higher *T*. Notably, a partial redistribution of B- and C-cations may explain the spectral changes in the range 100-400 $cm^{-1}$ which is dominated by *M*-O modes. Such a disorder is able to affect the geometry of the chains of $SiO_4$ tetrahedra and be responsible for the spectral changes observed in the range 500-1100 $cm^{-1}$. This mechanism is in full agreement with the changes in site populations derived from single-crystal structure refinement (SREF), which indeed indicate diffusion of Fe from the *M*(2) and the *M*(3) sites to the *M*(1) and the *M*(4) site (Oberti et al. 2018).

## Conclusions and implications

When spectroscopic data (sensitive to local structural fluctuations) are combined with the (long-range) XRD/SREF + Mössbauer data obtained during thermal annealing by Oberti et al. (2018), it becomes clear that the iron oxidation/deprotonation reaction in riebeckite is a multi-step process.

Figure 8 compares the temperature dependences of: (i) the normalized integrated OH-stretching absorption (FTIR annealing experiments); (ii) the unit-cell volume measured during heating/cooling by Oberti et al. (2018); (iii) the amount of $Fe^{2+}$ at *M*(1) and that of total $Fe^{3+}$ related to deprotonation measured by Mössbauer (Oberti et al. 2018). We can conclude that,

at the long-range scale (the crystal), the unit-cell volume drops in the temperature range 673-773 K, just after the onset of massive oxidation of ferrous irons, as evidenced by Mössbauer. The decrease in the unit-cell volume is mainly due to the shrinking of the *M*(1) octahedron, but is also favored by the simultaneous delocalization of $H^+$ within the *A* cavity and by changes in the average size and distribution of A and B cations (which mainly affect the *a* edge; Hawthorne and Oberti 2007). On the other hand, the integrated FTIR OH-stretching intensity drops at ~ 873 K, i.e., about 100 K beyond (Fig. 8).

In contrast, Raman analysis provides a very detailed picture of what happens at the short-range scale in a ~ 2 μm thick layer at the sample surface:

*Step 1* (~523 K < *T* < 623 K): reversible iron oxidation and $H^+$ delocalization. Figure 6 suggests that $H^+$ delocalizes ~ 523 K (cf. the peak in OH-stretching intensity), thus preceding (and prompting) $e^-$ delocalization, which occurs at ~ 623-648 K (cf. the peak in the 146 $cm^{-1}$ Raman scattering). Judging from the difference between the data collected on crystals S-110 and S-120, this dynamic and reversible process is probably dependent on the parameters used for thermal treatment. The *T* range of $e^-$ delocalization detected by Raman spectroscopy matches very well with the beginning of $Fe^{2+}$ oxidation detected by Mössbauer analysis (Fig. 8). Mössbauer spectroscopy is a bulk method, so that Figure 8 suggests that oxidation occurs simultaneously in the whole crystal, most probably because electrons are ~ 2000 times lighter than $H^+$. Raman spectra show that in the same *T* range, the $SiO_4$-ring geometry is dynamically and locally readjusted (Fig. 7).

*Step 2* (623 K < *T* < 723 K): because all electrons in the crystal are delocalized, a further increase in thermal energy increases the $e^-$ kinetic energy and promotes their ejection. Hence, above 723 K changes both in the Fe oxidation state and in the geometry of the double-chains of $SiO_4$ tetrahedra become irreversible and induce structural effects at the long-range scale, as evidenced by the shrinking of the unit-cell volume. Notably, this onset *T* seems not to be significantly affected by experimental parameters such as duration of thermal treatment and

sample size (i.e., powders *vs.* single crystals).

*Step 3* ($T \geq 823$ K): the process of irreversible oxidation is completed (no further change in the $Fe^{2+}/Fe^{3+}$ ratio according to Mössbauer spectroscopy is observed). Hence, all $H^+$ cations are forced to leave the crystal bulk as evidenced by the trend in the intensity of the OH signal collected (FTIR data, in Fig. 8).

In the present study we could reach the above conclusions only because we combined a number of techniques that are able to characterize different short-range and long-range properties under variable experimental conditions. However, considering that former studies done on synthetic potassic-ferro-richterite (Della Ventura et al. 2017) had shown a similar difference of ~ 100 K in the onset *T* detected by FTIR spectroscopy and XRD/SREF analysis, the proposed mechanism should be extended to all Fe-rich amphiboles.

As stated above, during this work, we observed no $H^+$ loss in riebeckite powders embedded in KBr pellets or in single-crystals treated under inert atmosphere, whereas pure powders and crystal fragments deprotonate readily in air. These observations thus confirm the mechanism proposed by reaction (1), where the release of $H^+$ is prompted by surficial (atmospheric) oxygen to form $H_2O$ molecules. The difference between the temperature of release of $H^+$ derived from single-crystal Raman scattering (surface sensitive) and IR absorption (bulk sensitive) is also in line with this scenario, and shows that the process starts at the crystal surface and proceeds through diffusion of both electrons and $H^+$ from the crystal core. Note also that during their experiments on riebeckite and arfvedsonite, Addison and Sharp (1962a) and Schmidbauer et al. (1996) had detected an electrical conductivity generated by a flux of electrons. One first implication of this study on geophysical models is that the deprotonation of amphiboles occurring at H*T* may explain the enhanced electrical conductivity measured in subducted slabs at convergent plate margins (Wang et al. 2012).

We have already done several isothermal experiments aimed at modeling the diffusion kinetics of $H^+$ across the amphibole matrix. The results of this work will be published

elsewhere after completing the experiments. However, we wish to anticipate here a result that is relevant to the present discussion. Figure 9 shows two FTIR-FPA (Focal Plane Array) images collected on a single crystal of riebeckite during an isothermal experiment done at 793 K. The two images were collected at R*T* on the same area of the sample at the beginning of the experiment (a) and after 80 min of thermal annealing (b). Whereas OH is homogeneously distributed in the untreated crystal (Fig. 9a), Figure 9b shows that 80 min of thermal annealing produce a thick (~70 μm) anhydrous rim but had virtually no effect on the OH content of the core. Indeed, this is a direct visual description of what we have discussed in the conclusions, i.e., that deprotonation starts at the crystal surface and proceeds towards the core with a kinetic rate still to be determined.

Previous work identified three possible crystal-chemical vectors responsible for the presence of $Fe^{3+}$ in the amphibole structure (e.g., Popp et al. 1990): (1) the process studied in this work, involving oxidation of $Fe^{2+}$ and loss of $H^{+}$; (2) the isovalent substitution $Al^{3+}Fe^{3+}_{-1}$ and (3) a substitution mechanism coupled to a vacancy at the A-site, i.e. $^{A}(Na,K)Fe^{2+A}\square_{-1}Fe^{3+}_{-1}$. This issue has significant implications for addressing the compositional variations of calcic amphiboles, such as hornblendes and kaersutites, and defining mantle metasomatism processes (Dyar et al. 1993). The experiments presented here clearly show that, in agreement with the conclusions of Dyar et al. (1993) based on the analysis of a large set of mantle-derived samples, the reaction (1) is the dominant process in controlling the final composition of Fe-rich amphiboles involved in high-temperature processes. Although conducted at $P$ = 1 atm, our results definitively show that reaction (1) is a very fast process, which however requires the presence of external oxygen to proceed.

A final and important implication of this work is that iron oxidation in riebeckite (and possibly in other Fe-rich silicates), is reversible within a definite but rather broad range of temperatures. In our knowledge, this is the first time that this peculiarity has been observed, and of course it might have interesting applications in materials science.

436

437 **ACKNOWLEDGMENTS**

438 Financial support by the Deutsche Forschungsgemeinschaft (1127/7-2) to BM and JS is
439 gratefully acknowledged. Thanks are due to Thomas Malcherek (Hamburg), for verifying the
440 crystallinity and determining the crystallographic orientation of the samples that were
441 subjected to in situ high-temperature Raman spectroscopy. Positive criticism of D. Jenkins
442 and M.D. Dyar improved the clarity of our manuscript.

443

444

## REFERENCES CITED

Addison, C.C., Addison, W.E., Neal, G.H., and Sharp, J.H. (1962a) Amphiboles. Part I. The oxidation of crocidolite. Journal of the Chemical Society, 1468-1471.

Addison, W.E., Neal, G.H., and Sharp, J.H. (1962b) Amphiboles. Part II. The kinetics of oxidation of crocidolite. Journal of the Chemical Society, 1472-1475.

Addison, W.E., and Sharp, J.H. (1962) Amphiboles. Part III. The reduction of crocidolite. Journal of the Chemical Society, 3693-3698.

Addison, W.E., and Sharp, J.H. (1968) Redox behavior of iron in hydroxylated silicates. Eleventh Conference on Clays and Clay Minerals. Abstracts, 95-104.

Addison, W.E., and White, A.D. (1968) The oxidation of Bolivian crocidolite. Mineralogical Magazine, 36, 791-796.

Aines, R.D., and Rossman, G.R. (1985) The high temperature behaviour of trace hydrous components in silicate minerals. American Mineralogist, 70, 1169-1179

Della Ventura, G., Marcelli, A., and Bellatreccia, F. (2014) SR-FTIR microscopy and FTIR imaging in the Earth Sciences. In, G.S. Henderson, D.R. Neuville, and R.T. Downs, Eds. Spectroscopic methods in Mineralogy and material Sciences, 78, p. 447-479. Reviews in Mineralogy and Geochemistry, Mineralogical Society of America, Chantilly, Virginia.

Della Ventura, G., Radica, F., Bellatreccia, F., Freda, C., and Cestelli Guidi, M. (2015a) Speciation and diffusion profiles of $H_2O$ in water-poor beryl: comparison with cordierite. Physics and Chemistry of Minerals, 42, 735-745.

Della Ventura, G., Radica, F., Bellatreccia, F., Cavallo, A., Cinque, G., Tortora, L., and Behrens, H. (2015b) FTIR imaging in diffusion studies: $CO_2$ and $H_2O$ in a synthetic sector-zoned beryl. Frontiers in Earth Science, 33, DOI: 10.3389/feart.2015.00033

Della Ventura, G., Susta, U., Bellatreccia, F., Marcelli, A., Redhammer, G., and Oberti, R. (2017) Deprotonation of Fe-dominant amphiboles: Single-crystal HT-FTIR

spectroscopic studies of synthetic potassic-ferro-richterite. American Mineralogist 102, 117-125.

Dowty, E. (1987) vibrational interactions of tetrahedra in silicate glasses and crystals. II. Calculations on melilites, pyroxenes, silica polymorphs and feldspars. Physics and Chemistry of Minerals 14, 122-138.

Dyar, M.D., Mackwell, S.J., McGuire A.V., Cross, L.R., and Robertson, J.D. (1993) Crystal chemistry of $Fe^{3+}$ and $H^{+}$ in mantle kaersutite: Implications for mantle metasomatism. American Mineralogist 78, 968-979.

Ernst, W.G., and Wai, M. (1970) Mössbauer, infrared, X-ray and optical study of cation ordering and dehydrogenation in natural and heat-treated sodic amphiboles. American Mineralogist, 55, 1226-1258.

Hawthorne, F.C., Oberti, R. (2007) Amphiboles: Crystal-chemistry. In F.C. Hawthorne, R. Oberti, G. Della Ventura and A. Mottana, Eds, Amphiboles: Crystal Chemistry, Occurrence and Health Issues, 67, 1-54. Reviews in Mineralogy and Geochemistry, Mineralogical Society of America, Chantilly, Virginia.

Hawthorne, F.C., Oberti, R., Harlow, G.E., Maresch, W.V., Martin, R.F., Schumacher, J.C. and Welch, M.D. (2012) Nomenclature of the amphibole supergroup. American Mineralogist, 97, 2031–2048.

Hodgson, A.A., Freeman, A.G., and Taylor, H.F.V. (1965) The thermal decomposition of crocidolite from Koegas, South Africa. Mineralogical Magazine, 35, 5-29.

Leissner, L., Schlüter, J., Horn, I., and Mihailova, B. (2015) Exploring the potential of Raman spectroscopy for crystallochemical analysis of complex hydrous silicates: I. Amphiboles. American Mineralogist, 100, 2682-2694

Momma, K. and Izumi, F. (2008) VESTA: a three-dimensional visulization system for electronic and structural analysis. Journal of Applied Crystallography, 41, 653-658.

Oberti, R., Boiocchi, M., Zema, M., and Della Ventura, G. (2016) Synthetic potassic-ferro-richterite: 1. Composition, crystal structure refinement and H*T* behavior by in operando single-crystal X-ray diffraction. Canadian Mineralogist, 54, 353-369.

Oberti, R., Boiocchi, M., Zema, M., Hawthorne, F.C., Redhammer, G.J., Susta, U., Della Ventura, G. (2018) The high-temperature behaviour of riebeckite: Expansivity, deprotonation, Fe oxidation and a novel cation disorder scheme. European Journal of Mineralogy, DOI: 10.1127/ejm/2018/0030-2712.

Phillips, M.W., Popp, R.K., and Clowe, C.A. (1988) Structural adjustments accompanying oxidation-dehydrogenation in amphiboles. American Mineralogist, 73, 500-506.

Phillips, M.W., Draheim, J.E., Popp, R.K., Clowe, C.A., and Pinkerton, A. A. (1989) Effect of oxidation-dehydrogenation in tschermakitic hornblende. American Mineralogist, 74, 764-773.

Phillips, M.W., Popp, R.K., and Clowe, C.A. (1991) A structural investigation of oxidation effects in air-heated grunerite. American Mineralogist, 76. 1502-1509.

Popp, R.K., Phillips, M.W., and Harrell, J.A. (1990) Accomodation of $Fe^{3+}$ in natural $Fe^{3+}$-rich calcic and subcalcic amphiboles: Evidence from published chemical analyses. American Mineralogist, 75, 163-169.

Schmidbauer, E., Kunzmann, Th., Fehr, Th., Hochleitner, R. (1996) Electrical conductivity, thermopower and $^{57}Fe$ Mössbauer spectroscopy on an Fe-rich amphibole, arfvedsonite. Physics and Chemistry of Minerals, 23, 99-106.

Susta, U., Della Ventura, G., Hawthorne, F.C., Abdu, Y.A., Day, M.C., Mihailova, B., Oberti, R. (2018) The crystal-chemistry of riebeckite, ideally $Na_2Fe^{2+}{}_3Fe^{3+}{}_2Si_8O_{22}(OH)_2$: a multidisciplinary study. Mineralogical Magazine, DOI:10.1180/minmag.2017.081.064

Turci, F., Tomatis, M., Pacella, A. (2017) Surface and bulk properties of mineral fibres relevant to toxicity. In A.F. Gualtieri, Ed., Mineral fibres: crystal chemistry, chemical

physical properties, biological interaction and toxicity. EMU Notes in Mineralogy, 18, 171–214.

Ungaretti, L. (1980) Recent developments in X-ray single crystal diffractometry applied to the crystal-chemical study of amphiboles. Godisnjak Jugonslavenskog Centra za Kristalografiju, 15, 29-65.

Wang, D., Guo, Y., Yu, Y., Karato, S. (2012) Electrical conductivity of amphibole-bearing rocks: influence of dehydration. Contribution to Mineralogy and Petrology, 164, 17-25.

Watenphul, A., Malcherek, T., Wilke, F., Schlüter, J., Mihailova, B. (2017) Composition–thermal expandability relations and oxidation processes in tourmaline studied by in-situ Raman spectroscopy, Physics and Chemistry of Minerals, 44, 735-748.

Zang, M., Wang, L., Hirai, S., Redfern, S.A., and Salje, E.K.H. (2005) Dehydrohylation and $CO_2$ incorporation in annealed mica (sericite): an infrared spectroscopic study. American Mineralogist, 90, 173-180.

Zang, M., Hui, Q., Lou, X.J., Redfern, S.A., Salje, E.K.H., and Tarantino, S.C. (2006) Dehydrohylation, proton migration, and structural changes in heated talc: an infrared spectroscopic study. American Mineralogist, 91, 816-825.

## FIGURE CAPTIONS

**Figure 1.** (a) The *C*2/*m* amphibole structure of the studied riebeckite. $SiO_4$ tetrahedra are given in blue, *M*(1) octahedra in olive-green, *M*(2) in gray, *M*(3) in light blue, the *M*(4) site in violet, the *A* site in yellow; the dashed contour marks the OH group occurring at the O(3) sites. (b) local structure configurations around the anionic O(3) site: at low *T*, all the *M*(1,3) octahedra host ferrous iron and coordinate two OH groups; at high *T*, ferrous iron occurring at both the *M*(1) octahedra (in olive green) oxidizes to ferric iron, the local charge balance being restored by the $OH^- \rightarrow O^{2-}$ reaction. The reaction is reversible for $T < 723$ K. Figures prepared using VESTA (Momma and Izumi 2008).

**Figure 2.** OH-stretching FTIR spectra measured (a) at R*T* after quenching from any target *T* (in Kelvin), and (b) in situ on a 135 μm-thick doubly-polished section. For the sake of clarity, the spectra are plotted with the same absorbance scale and offset for the vertical axis.

**Figure 3.** Temperature dependence of integrated OH-stretching IR absorbance normalized to the IR absorbance at R*T*. 135 μm thick doubly-polished section. The uncertainties in the data points are within the size of the symbols.

**Figure 4**. Parallel polarized Raman spectra measured at increasing *T* from crystal surfaces parallel to $(\bar{1}10)$ (left) and $(\bar{1}20)$ (right), respectively, with [001] always perpendicular to the polarization of incident light; R*T* = room temperature. For the sake of clarity, the spectra have been offset vertically and the same color is maintained at each temperature value.

**Figure 5**. The range of *M*-O modes in selected Raman spectra measured in situ at different temperatures. For the sake of clarity, the spectra have been offset vertically.

**Figure 6**. Temperature dependence of the total Raman intensity ($total\ I^{Raman}_{\mathrm{OH\,stretching}}$) of the OH-stretching modes (a and d), of the Raman signal near 146 $cm^{-1}$ normalized to the total intensity in the range 15-1215 $cm^{-1}$ ($I_{n\ 146cm^{-1}}$; b and e) and of the Raman intensity ratio $I_{165cm^{-1}}/(I_{165cm^{-1}} + I_{173cm^{-1}})$ which are all related to *M*(1)-O vibrations. The error bars in 6b and 6e are within the size of the symbols.

571 **Figure 7.** The temperature dependence of the wavenumber $\omega$ (circles) and FWHM $\Gamma$
572 (squares) of the $SiO_4$-ring mode near 665 $cm^{-1}$ (a and c) and of the $SiO_4$-stretching mode near
573 971 $cm^{-1}$ (b and d). For the sake of simplicity, the intermediate data points collected from S-
574 110 on cooling in the first temperature ramp and in the second ramp have been omitted. The
575 color code is the same as in Fig. 6.
576
577 **Figure 8**. Comparison of the temperature dependence of: (a) the FTIR intensity of the OH-
578 stretching band, (b) the unit-cell volume (from Oberti et al., 2018), where points collected
579 (during heating) on the protonated crystal are in blue and those on the deprotonated crystal are
580 in green; (c) Mössbauer data showing the relation of the $Fe^{2+}$ content at *M*(1) with the total
581 $Fe^{3+}$ (data from Oberti et al., 2018). The error bars are within the size of the symbols. See text
582 for more details.
583
584 **Figure 9**. FTIR-FPA images of a doubly polished single crystal of the studied riebeckite,
585 thickness 110 μm. (a) before the heating run, (b) quenched after 80 min at 793 K. The images
586 were collected using a 64x64 pixel FPA detector coupled with a 15x Schwarzschild objective
587 and installed on a Bruker Hyperion 3000 FTIR microscope. The nominal resolution is 4 $cm^{-1}$
588 and 128 scans were averaged for both background and sample. With this set-up, we could
589 collect simultaneously 1024 spectra covering an area of 174 x 174 μm with a spatial
590 resolution close to 5 μm (Della Ventura et al. 2014). The OH signal was integrated in the
591 whole 3590-3670 $cm^{-1}$ range. Colors are proportional to the intensity scale: red = maximum,
592 blue = minimum (zero intensity). The *c* crystallographic direction is indicated by the arrow,
593 the white broken line in (b) indicates the crystal rim.
594

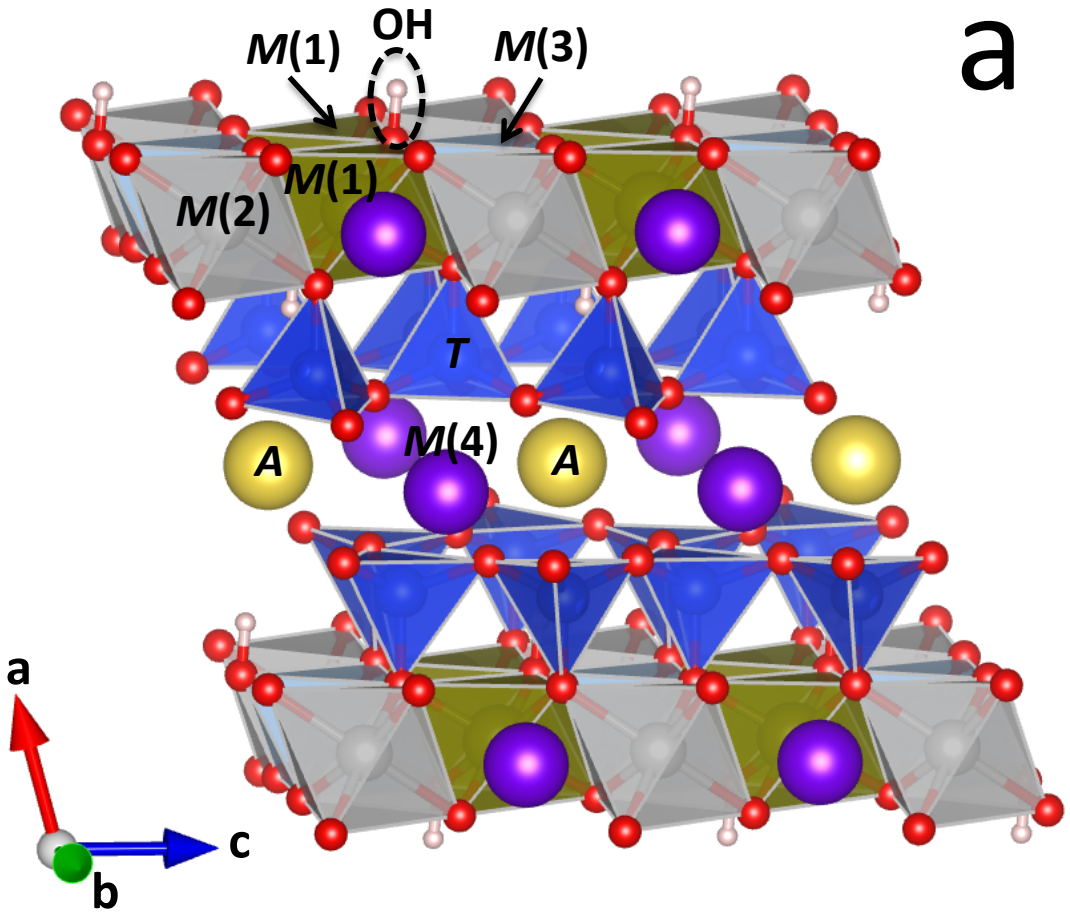
a
M(1)
OH
M(3)
M(1)
M(2)
T
M(4)
A
A
a
c
b

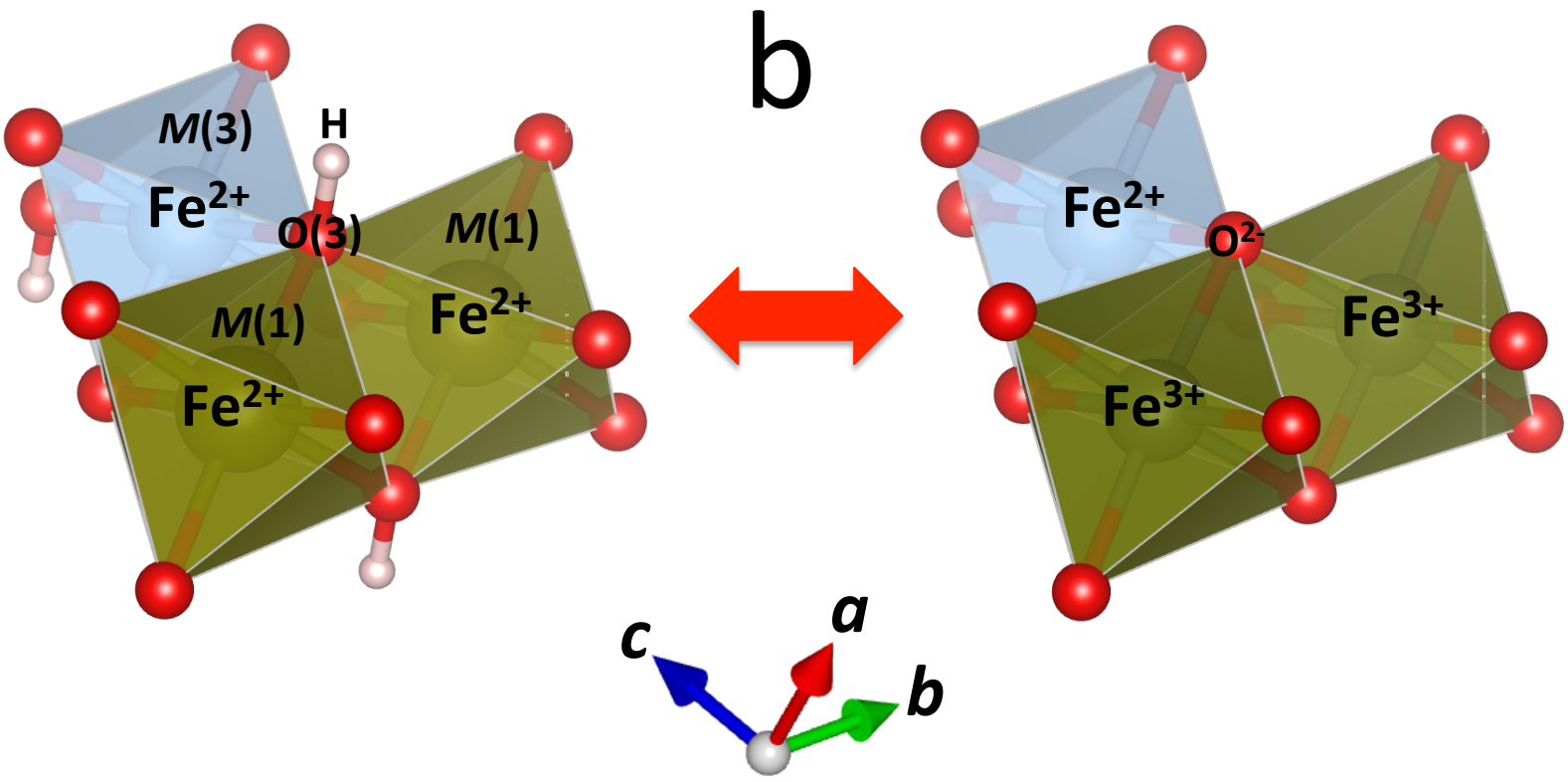
b
M(3)
H
Fe2+
O(3)
M(1)
M(1)
Fe2+
Fe2+
Fe2+
O2-
Fe3+
Fe3+
c
a
b

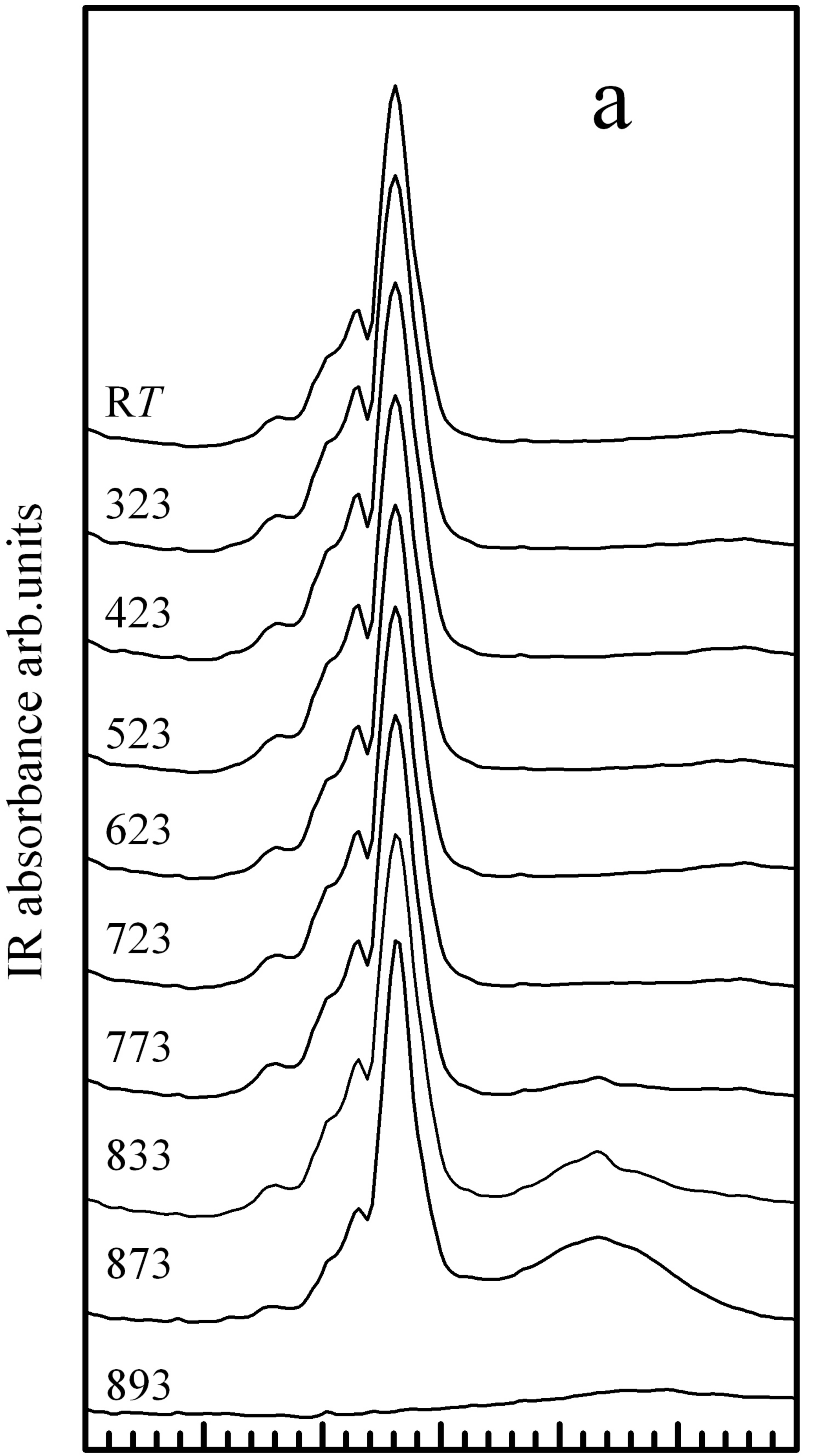
a
RT
323
423
523
623
723
773
833
873
893
IR absorbance arb.units
3750
3700
3650
3600
3550
3500
3450
wavenumber (cm-1)

b

RT

343

423

523

623

723

773

833

873

893

IR absorbance arb.units

3750 3700 3650 3600 3550 3500

wavenumber ($cm^{-1}$)

in situ
quenched
$Int_T/Int_{RT}*100$
Temperature (K)
0
50
100
150
200
250
300
400
500
600
700
800
900
1000

S-110

S-120

Intensity (counts/s)

RT, *final*
773 K
423 K
623 K
RT
423 K
573 K
723 K
673 K
623 K
573 K
971
423 K
146
165
173
665
3619
RT, *initial*

798 K
773 K
723 K
703 K
683 K
673 K
663 K
623 K
573 K

Raman shift ($cm^{-1}$)

S-110

S-120

RT, *final*

723 K

673 K

623 K

RT, *initial*

146

165

173

Intensity (counts/s)

Raman shift ($cm^{-1}$)

S-110

S-120

(a)

rate 10 K/min

heating, first ramp

2nd ramp:
heating 623 K
cooling 423 K
heating 773 K

cooling,
first ramp

final cooling

total $I^{Raman}_{OH\ stretching}$ (counts/s)

(b)

$I_{n\ 146cm^{-1}}$

(c)

$I_{165cm^{-1}}/(I_{165cm^{-1}}+I_{173cm^{-1}})$

Temperature (K)

(d)

rate 50 K/min

rate 10 K/min

heating

cooling

total $I^{Raman}_{OH\ stretching}$ (counts/s)

(e)

$I_{n\ 146cm^{-1}}$

(f)

$I_{165cm^{-1}}/(I_{165cm^{-1}}+I_{173cm^{-1}})$

Temperature (K)

S-110

(a)

wavenumber $\omega_{665cm^{-1}}$ ($cm^{-1}$)

FWHM $\Gamma_{665cm^{-1}}$ ($cm^{-1}$)

Temperature (K)

(b)

wavenumber $\omega_{971cm^{-1}}$ ($cm^{-1}$)

FWHM $\Gamma_{971cm^{-1}}$ ($cm^{-1}$)

Temperature (K)

S-120

(c)

wavenumber $\omega_{665cm^{-1}}$ ($cm^{-1}$)

FWHM $\Gamma_{665cm^{-1}}$ ($cm^{-1}$)

Temperature (K)

(d)

wavenumber $\omega_{971cm^{-1}}$ ($cm^{-1}$)

FWHM $\Gamma_{971cm^{-1}}$ ($cm^{-1}$)

Temperature (K)

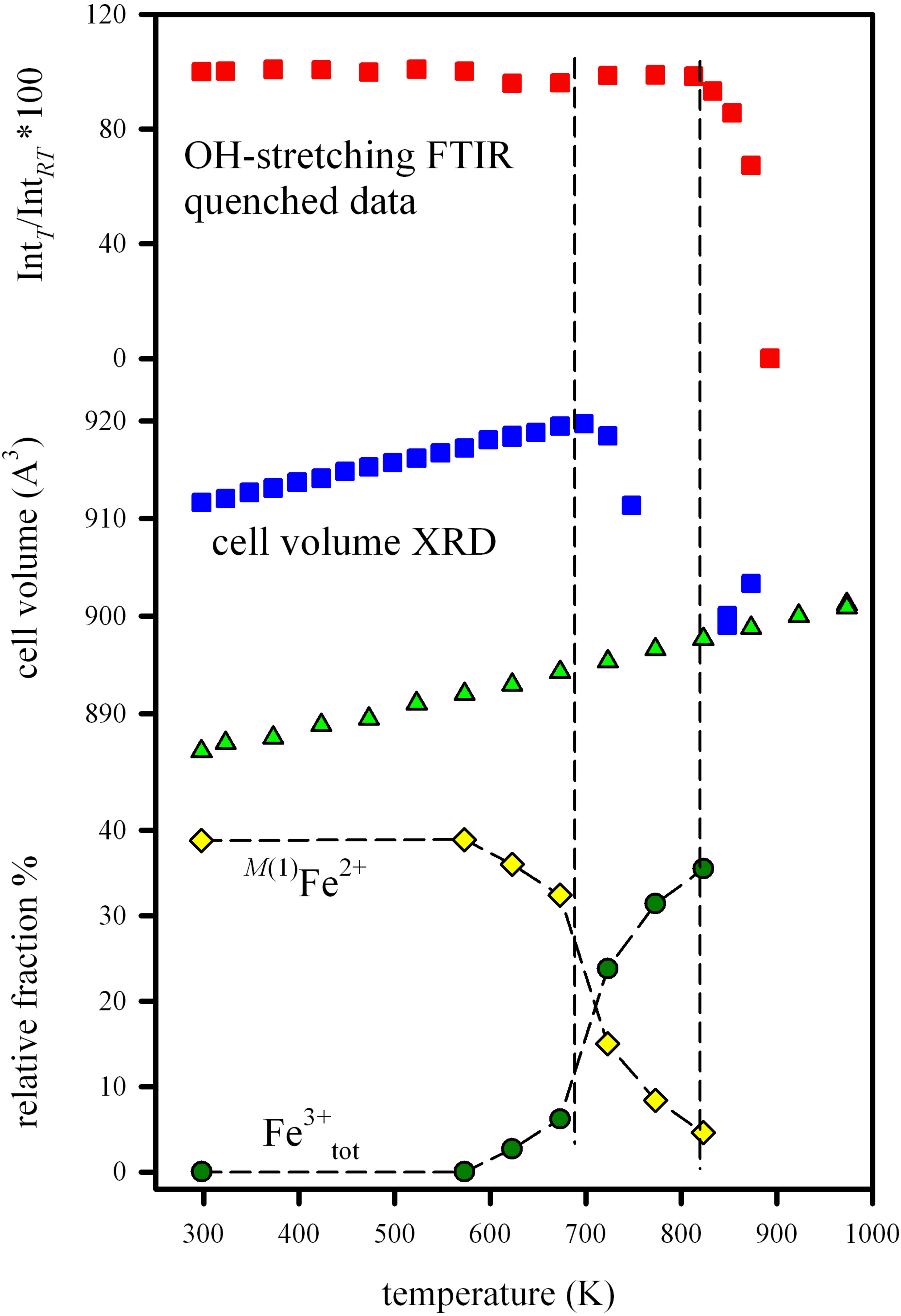
120
80
40
0
920
910
900
890
40
30
20
10
0
$Int_T/Int_{RT}*100$
cell volume ($A^3$)
relative fraction %
OH-stretching FTIR
quenched data
cell volume XRD
$M(1)Fe^{2+}$
$Fe^{3+}_{tot}$
300
400
500
600
700
800
900
1000
temperature (K)

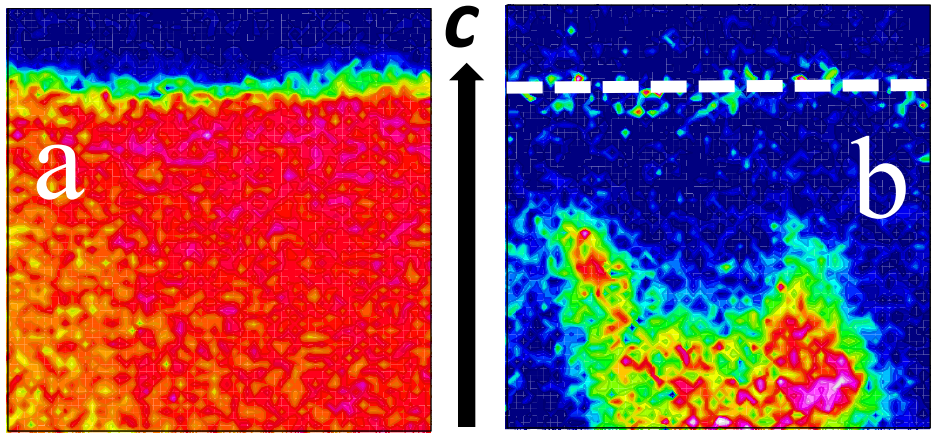
a
c
b